



Room-temperature tilted-target sputtering deposition of highly transparent and low sheet resistance Al doped ZnO electrodes

Journal:	<i>Journal of Materials Chemistry C</i>
Manuscript ID:	TC-ART-03-2015-000695.R1
Article Type:	Paper
Date Submitted by the Author:	14-Apr-2015
Complete List of Authors:	Nagiri, Ravi; The University of Queensland, Centre for Organic Photonics & Electronics Yambem, Soniya; The University of Queensland, Centre for Organic Photonics & Electronics Lin, Qianqian; The University of Queensland, Centre for Organic Photonics & Electronics Burn, Paul; The University of Queensland, Centre for Organic Photonics & Electronics Meredith, Paul; University of Queensland, Centre for Organic Photonics and Electronics

Room-temperature tilted-target sputtering deposition of highly transparent and low sheet resistance Al doped ZnO electrodes

Ravi Chandra Raju Nagiri,[†] Soniya D. Yambem,[†] Qianqian Lin, Paul L. Burn* and Paul Meredith*

Centre for Organic Photonics & Electronics
The University of Queensland, Queensland 4072, Australia

E-mail: *p.burn2@uq.edu.au, *meredith@physics.uq.edu.au

[†] RCRN and SDY contributed equally to the manuscript.

Abstract

Target tilted room temperature sputtering of aluminum doped zinc oxide (AZO) provides transparent conducting electrodes with sheet resistances of $<10 \Omega \square^{-1}$ and average transmittance in the visible region of 80-84%. The properties of the AZO electrode are found to be strongly dependent on the target-tilting angle and film thickness. The AZO electrodes showed comparable performance to commercial indium tin oxide (ITO) electrodes in organic photovoltaic (OPV) devices. OPV devices containing a bulk heterojunction active layer comprised of poly(3-*n*-hexylthiophene-2,5-diyl) (P3HT):phenyl-C61-butyric acid methyl ester (PCBM) and AZO transparent conducting electrode had a power conversion efficiency (PCE) of up to 2.5% with those containing ITO giving a PCE of 2.6%. These results demonstrate that AZO films are a good alternative to ITO for transparent conducting electrodes.

1. Introduction

The development of alternative transparent conducting electrodes to replace indium tin oxide (ITO) is necessary to meet the rapid developments in organic optoelectronics including application in solar cells [1-3] and light-emitting diodes [4,5] and the predicted future scarcity of indium [6]. The bench mark for any new electrode is the performance of commercial ITO (UV-visible transmission (T) > 80% & sheet resistance (R_{sh}) < 20 Ωsq^{-1}) with an added requirement of room-temperature processing [7]. However, it is important to note that glass, which is the most widely used substrate, has ~ 9-10% loss in UV-visible transmission due to Fresnel reflection (air-glass interface) and absorption losses. Thus electrodes on glass should have a maximum transmission of around 90% in the visible region (400- 800 nm) unless they also have the capability of an anti-reflection coating. Surprisingly, there are reports in which transparent conducting electrodes have optical transmittances of >90% [8-10]. Such reports must be viewed with caution since the electrode materials in question have refractive indices greater than glass and hence do not form anti-reflection coatings.

Evolving strategies for ITO electrode replacement include: oxide based sandwich structures with metallic mid layers [11-15]; carbon, metal nanowire networks [16-22]; binary or ternary oxides [23-28]; graphene [29, 30]. The main contribution to transmission loss (absorption) in TCO electrodes are the dopants in the host oxide matrices, oxygen vacancies, interstitial defects, and free carriers [e.g., aluminium in zinc oxide for aluminium zinc oxide (AZO)]. Recently, Kim et al, [31] reported the increase in optical transmission through defect passivation in AZO by co-doping fluorine (F) and hydrogen (H). This led to better performing organic photovoltaic (OPV) and organic light-emitting diode (OLED) devices compared to conventional ITO-electrode controls. The underlying principle of increasing the transmission was the replacement of oxygen sites with other anions in the valence band of the host oxide to improve the carrier mobility and optical transmittance without disturbing the carrier concentration in the conduction band [32]. However, first-principle calculations on the F doped ZnO system reveal that these dopants can not be activated at room temperature, [33] and therefore the electrodes were prepared at 150 °C and annealed at 300 °C post deposition. Thus, a room temperature method for fabricating TCO electrodes with equal or better optoelectronic properties equivalent or superior to ITO is still a challenge.

AZO continues to be a system of considerable interest due to the abundance of aluminium and zinc relative to indium [34]. Approaches to the preparation of AZO electrodes have included solution and vacuum deposition methods. For example, preparation of AZO by aqueous solution processing has been reported by Hagendorfer et al [35]. The AZO electrodes formed had a thickness of 2 μm and a sheet resistance in the range 25 to 40 Ωsq^{-1} , and transmission of 75 to 85%. They achieved these optoelectronic characteristics by activating the dopants with UV light at ~80 °C. Another promising technique for AZO deposition is pulsed laser deposition (PLD). The advantage of PLD lies in the creation of a very dense plasma by interaction of a high energy pulsed laser beam with the target material leading to denser, higher mobility films. Using pulsed laser deposition Franklin et al [36] reported the best sheet resistance for AZO electrodes thus far (17 Ωsq^{-1}) and T ~ 75 to 85%. The films had a thickness of 620-680 nm and were deposited at 150 °C. Although the PLD method can give

AZO with good optoelectronic properties, it is not easily scaled for large area deposition and the films often contain particulates, which can lead to shorting of devices.

Recently, facing target sputtering (FTS), in which two targets are facing each other in the sputtering chamber and the substrate is situated in a plane perpendicular (above or below) to the targets, has been used to deposit TCOs [37]. The advantage of this technique is that by keeping the targets face-to-face, a dense plasma can be created while at the same time bombardment of the substrate by the high energy plasma species is reduced. This method thus has the potential to enable electrode fabrication at low temperatures with good optoelectronics properties as the carrier mobility is improved due to high density of the plasma. Using FTS Jeong et al [37] reported room temperature deposited AZO on polyethylene terephthalate (PET) with a sheet resistance of $45 \pm 9 \Omega \square^{-1}$ and transmission of 85% for a 300 nm thick film. Additionally, an AZO electrode was reported by Jung et al [38] that had a sheet resistance of $30 \Omega \square^{-1}$ and transmission of 90% in the visible. The film was again grown by FTS at room temperature but in this case it was deposited on polycarbonate (PC) and was 300 nm thick. However, while the optical properties of these materials were acceptable, the sheet resistances were still below that of commercial ITO. Further, FTS systems have a high material wastage which needs to be improved to reduce target consumption.

In this manuscript we report AZO electrodes deposited at room temperature with very low sheet resistance ($< 10 \Omega \square^{-1}$) and high transmission ($> 80\%$, in the visible). To the best of our knowledge, this is the best sheet resistance and transmittance combination for room temperature grown AZO thus far. The optimised AZO electrodes were achieved by controlling the target tilt with respect to the plane of the substrate while depositing the films. Furthermore, we show that OPV devices incorporating these electrodes had comparable performance to those using commercial ITO.

2. Materials and Methods

2.1. Electrode Preparation and Characterization

The AZO electrodes were prepared using an AJA International magnetron sputtering system. The sputtering target used for the deposition was a 4" diameter circular ceramic target [ZnO (99.999%) doped with 2 wt% Al_2O_3 (99.99%)] purchased from AJA international, USA. *In-situ* glass substrate (Cat-I Glass, Illinois, USA) cleaning was done in an argon plasma (30 mTorr, 70 watt radio frequency) for 5 min prior to the AZO electrode deposition. The base pressure in the chamber was kept 1×10^{-7} Torr. The distance between substrate and target was 15 cm and the substrate-holder was rotated at a constant speed of 20 rpm during sputtering. No external substrate heating was used for the electrode deposition during or post deposition. Deposition was carried out at 1 mTorr of argon pressure (based on studies reported by Treharne *et al.*, [39]) and with a 200 watt radio frequency power supply. The thickness of the electrodes was measured in two ways: *in-situ* quartz crystal monitor (in-built with AJA sputtering system), and ellipsometry after deposition.

A variable angle spectroscopic ellipsometer (J.A.Woollam WASE VB-400) was used to analyze thicknesses, refractive index, and extinction coefficients of the electrodes. Tauc-Lorentz and Drude dispersion models are applied to fit the ψ/Δ

ellipsometry data for extracting the optical constants. A mean square error (MSE) of <5 with the fitting models implies that the extracted fitting parameters are accurate. A UV-Vis-NIR absorption spectrophotometer (Cary 5000) was used to measure the optical transmission of the films which was corrected for the substrate (glass) absorption/reflection losses (~9-10%). Mean, maximum and minimum values of transmission were calculated for the visible wavelength range 400 nm to 800 nm. Sheet resistance and resistivity were measured using a KeithLink probe-measurement setup using a Keithley (Model No: 2100) 6-1/2 digital measurement multimeter. Carrier type and concentration, mobility and conductivity were measured using an Ecopia HMS-3000 Hall measurement system (0.56 Tesla magnetic field strength) in a van der Pauw geometry at room-temperature. Gold paste (99.999% purity) was used to make 4 contacts on the electrode edges so that the contact resistances could be neglected. Ohmic behavior of the Au contact to the AZO electrodes was confirmed prior to the Hall measurements by observation of the linear variation in the I-V curves. X-ray diffraction (XRD) spectra of the AZO films were collected on a Bruker Advance D8 X-Ray Diffractometer equipped with a LynxEye detector, Cu tube ($\text{Cu K}_\alpha = 1.5418 \text{ \AA}$) and operated at 40 kV with a 2θ scan range of 20-80°. Surface morphology, cross-sectional images and energy dispersive X-ray spectroscopy (EDX) measurements were performed using a Jeol JSM-7100F field-emission scanning electron microscopy (FESEM) with an accelerating voltage of 1 keV. The surface roughness of the films was measured by atomic force microscopy (AFM, Asylum research MFP 3D) in contact mode.

2.2. OPV Device Modelling, Fabrication and Characterization

2.2.1. Optical Modelling. The optical field distributions and short circuit current under AM1.5G solar illumination were modeled using a Matlab code developed by Burkhard et al. [40] based on a transfer matrix method described by Pettersson et al. [41]. For these simulations optical constants (refractive index and extinction coefficients) of all the materials in the structure are required (**Figure S2**). Spectroscopic ellipsometry (SE) measurements of AZO on silicon wafers were performed to determine the optical constants of the AZO films.

2.2.2. Fabrication. Pre-patterned ITO substrates (Xinyan Technology Ltd.) were prepared for device fabrication using a multi-step cleaning process. First, the substrates were washed with Alconox in de-ionized water by rubbing it with a lint free swab. The substrates were then rinsed several times with de-ionized water and ultra-sonicated in the same for 5 minutes. This was followed by consecutive ultra-sonication in acetone and 2-propanol for 10 minutes each. The substrates were dried using a nitrogen gun. 10 nm of MoOx (Sigma Aldrich) was deposited using a vacuum thermal evaporator at a base pressure $\sim 10^{-6}$ mbar onto the cleaned ITO and AZO electrodes. For the P3HT:PCBM photoactive layer, a blend of P3HT:PCBM (1:1 w/w) was prepared by mixing equal amounts of individual solutions of P3HT (Merck, Mw = 94 kDa, PDI = 1.9) and PCBM (American Dye Source) in dichlorobenzene (DCB) (anhydrous grade). Both individual solutions had a concentration of 30 mg (mL)⁻¹. The P3HT:PCBM blend was then filtered (0.22 μm PTFE filter, Membrane Solutions) and spin-coated (500 rpm for 3 s, then 1400 rpm for 17 s) on top of AZO/MoOx or ITO/MoOx. The films were then annealed on a hot plate at 60 °C for 20 minutes. Finally, 100 nm of Al was deposited using a thermal evaporator at a pressure $\sim 10^{-6}$ mbar to complete the

device structure. The devices had an active area of 0.2 cm^2 , which was defined using a shadow mask. Post fabrication, the devices were annealed on a hot plate for 2 minutes at $180 \text{ }^\circ\text{C}$.

2.2.3. Characterization. The device characteristics were tested using an Abet Triple-A (Abet Technologies) solar simulator as the light source. The solar mismatch of the Xenon lamp (550 W Oriel) spectrum was minimized using an AM1.5G filter. Light intensity at $\approx 100 \text{ mW cm}^{-2}$ AM1.5G was calibrated using a National Renewable Energy Laboratory (NREL) certified standard silicon photodiode (2 cm^2), with a KG5 filter. A Keithley 2400 source-measurement unit was used for the current density-voltage (JV) measurements. JV characteristics were measured for at least five devices in each category. A PV Measurement QEX7 setup, which was calibrated with an NREL certified photodiode and operated without white light bias and chopped and locked in the small perturbation limit, was used for recording IPCE spectra for the best devices in each category. The average of difference between short circuit current density from JV measurements and integrated current density from IPCE were within 10%.

All fabrication steps and testing of devices were done in a class 1000 cleanroom. Except for cleaning of ITO substrates, all other steps on device fabrication and testing on ITO and AZO electrodes were done in an inert environment (MBraun glove box, $\text{O}_2 < 0.1 \text{ ppm}$; $\text{H}_2\text{O} < 0.1 \text{ ppm}$). The evaporations were done using a thermal evaporator connected to a glove box.

3. Results and discussion

3.1. AZO electrodes

The development of the room temperature sputter deposited AZO electrodes was performed in two stages. First, the target tilt angle was optimized to achieve the best combination of sheet resistance and transmittance, and then second, using the best target tilt angle the optoelectronic properties were fine-tuned by varying the thickness of AZO films. To reiterate, it is important to note that all the electrodes used in this study were prepared at room-temperature without using any heat treatment during deposition, such as substrate-heating, or thermal annealing post deposition. A schematic of the target-substrate geometry is shown in **Figure 1a**, demonstrating the target tilt angles with respect to substrate plane and plasma profile distribution.

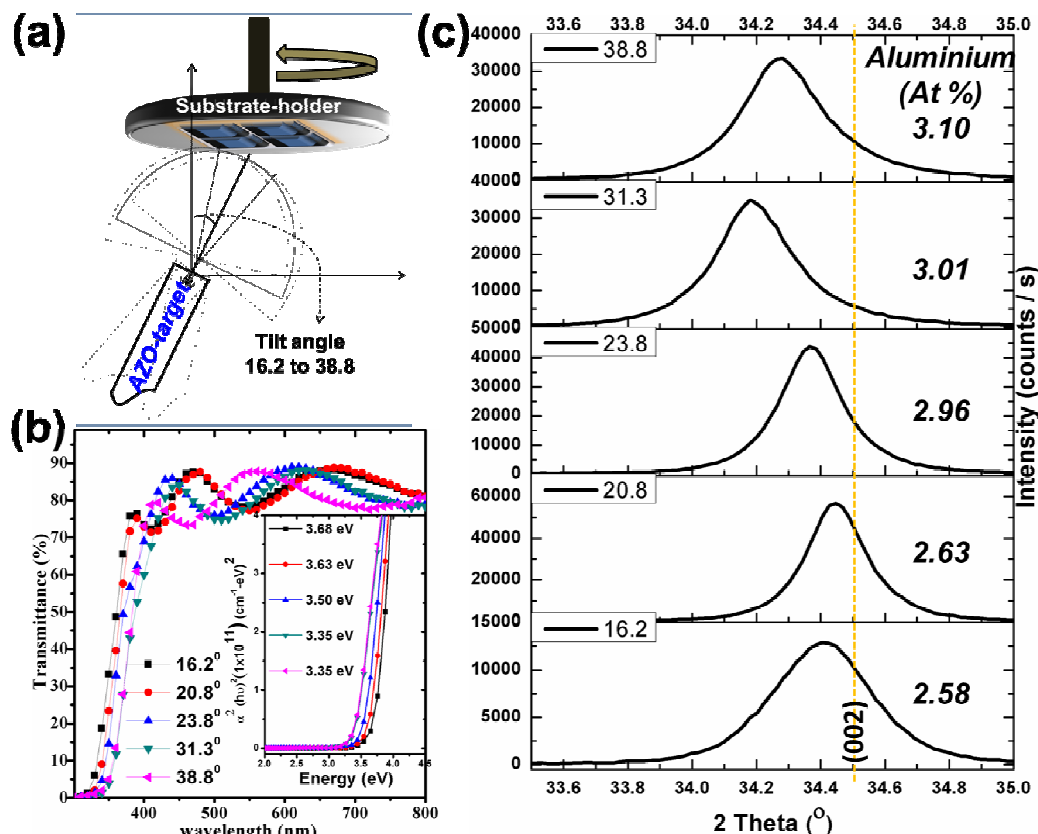


Figure 1. a) Schematic representation of target tilt angle with respect to the substrate. b) Substrate (glass)-corrected optical transmission spectra collected for the AZO films prepared at target tilt angles of 16.2°-38.8°, the in-set of the figure shows the direct optical band gap Tauc-plot for the AZO films and corresponding extracted bandgap values. c) XRD patterns of the AZO films with in-sets showing the Al ion concentration in the films estimated from EDAX measurements.

3.2 Effect of target tilt angle

When the target tilt was varied from 16.2° to 38.8° the deposition rate of AZO was found to increase linearly from 2.4 to 4.8 nm min⁻¹ with a constant target-sputtering power, which indicates significant changes in the density of the incoming plasma from the AZO target onto the substrate. From the X-ray diffraction (XRD) characterization of these films, as shown in **Figure 1c**, it can be seen that the films had a hexagonal wurtzite crystal structure. The film growth had a preferential *c*-axis orientation along the (002) plane perpendicular to the substrate, with values of 2θ that are lower than the ZnO bulk (002) diffraction line at 34.5° [42]. The lower 2θ values for the AZO films are a result of intrinsic stress developed at the glass-AZO film interface during the sputtering process. For cases of films on glass ($h/H \ll 1$, where *H* and *h* are substrate and film thicknesses, respectively), the intrinsic stress is mainly due to the non-equilibrium film-growth conditions and not due to temperature or lattice mismatch. In general, any redistribution of matter on the substrate will result in film stress, since the film is constrained by the substrate [43]. In addition, for films grown from the Al-doped zinc oxide ceramic targets used in this work, Al incorporation into the film should not be neglected since it also influences the crystal lattice constant and therefore changes 2θ . From **Figure 1c** it can be seen that the aluminium concentration in the resultant AZO films increases

with increasing target tilt angle (from 16.2° to 38.8°) as a result of the increase in the deposition rate. If the Al³⁺ (52 pm ionic radius) ions present in the film completely replaced the Zn²⁺ (72 pm) sites, the resultant AZO crystal lattice constants would be expected to be reduced leading to a smaller interplanar spacing and, according to Bragg's law, 2θ should shift to higher values [44]. However, this is not seen in the AZO films shown in **Figure 1c** and arises from the fact that the AZO films grown at room temperature do not have sufficient activation energy for the Al-atoms to replace the Zn-sites but instead the Al atoms reside in the films as interstitial ions. Therefore, the lower 2θ values observed for the AZO films formed with increasing tilting angles signifies that the stress was caused predominantly by the interstitial Al atoms and not Zn interstitials or oxygen vacancies.

We further investigated the stress in the films using a biaxial strain model [45], with the estimated stress developed in the plane of the AZO film shown in **Table 1**.

Table 1. Physical properties of the AZO films prepared at target tilt angles ranging from 16.2° to 38.8° determined from XRD, Hall-effect, four-point probe, optical absorption spectroscopy and spectroscopic ellipsometry measurements describing average values.

Target tilt	t [nm] ±5	Al [At %]	d [Å]	Area of (002) XRD peak	C [Å]	σ [GPa]	R_{sh} [$\Omega \square^{-1}$]	n [cm ⁻³]	μ [cm ² V ⁻¹ s ⁻¹]	E_g [eV] ±0.02
16.2°	353	2.68	2.605	5136	5.211	-0.13	25	4.23×10 ²⁰	17.2	3.68
20.8°	362	2.63	2.602	58845	5.203	+0.13	40	2.89×10 ²⁰	14.7	3.63
23.8°	321	2.96	2.607	14825	5.214	-0.36	81	1.99×10 ²⁰	11.8	3.50
31.3°	322	3.01	2.620	14481	5.240	-1.52	458	6.76×10 ¹⁹	6.5	3.35
38.8°	290	3.10	2.614	14786	5.227	-0.94	544	7.78×10 ¹⁹	5.4	3.35

Negative values of stress correspond to compressive stress and positive values correspond to tensile stress in the film. The AZO films prepared at different target tilting angles showed compressive stress except for the films prepared at an angle of 20.8° (**Table 1**). The difference for the case of the 20.8° films is mainly due to the relatively high film thickness (362 nm), which may be larger than the critical thickness where compressive stress converts to tensile stress due to the crystal coalescence. The greater film thickness of the AZO deposited with a tilting angle of 20.8° is also evident in the higher peak intensity value in the XRD spectra (**Table 1**) compared to all other films. Typical behaviour of the average film stress as a function of film thickness shows a transition from compressive to tensile and then to relaxed states [43]. Tensile stress is seen in AZO films with higher thickness (> 400 nm) and this will be further discussed later. **Figure 1b** shows optical

transmission spectra of AZO films versus variation in the target tilt angle. The wavelength position of the interference fringes for each of the films is due to the different optical thicknesses of the AZO.

The transmission spectra and electrical parameters for the AZO films formed using different target tilt angles are shown in **Figure 1(b)** and **Table 1**, respectively. Hall-effect measurements showed n-type conductivity for all the films. The carrier (electrons) concentration of the films was found to decrease with increasing target tilt angle and it is not surprising that the optical band gap also followed the same trend. Band-gap variation with respect to the carrier density is very well understood for doped semiconductors, and arises mainly from band gap renormalisation effects above the Mott critical carrier density limit, which is $3.68 \times 10^{18} \text{ cm}^{-3}$ in the case of ZnO [46]. The carrier concentration of all the AZO films in this study showed values above the Mott limit (**Table 1**) and there is an increase in electron carrier concentration in the AZO films with a decrease in the target tilting angle. In the AZO of this work, the increase in electron carrier concentration can be correlated to the amount of donors: oxygen vacancies, and Al and Zn metal interstitials present inside the films.

Similar to the trend for carrier concentration, the Hall-mobility also increased with the decrease in target tilt angle. It is well known that the mobility of carriers in TCOs are mainly related to macroscopic (grain boundaries, surface roughness) and microscopic (ionized donors, neutral impurities) imperfections in the films [47]. For the AZO films the decrease in mobility with increased target tilt angles can be directly correlated to both the stress (estimated from the XRD data as discussed earlier) and surface roughness. Surface roughness values for AZO films extracted from modelling of thickness data showed increased roughness with larger target tilt angles (**Table S2**). Scanning electron microscopy (SEM) images of the AZO films formed using different target tilt angles are shown in **Figure 2**.

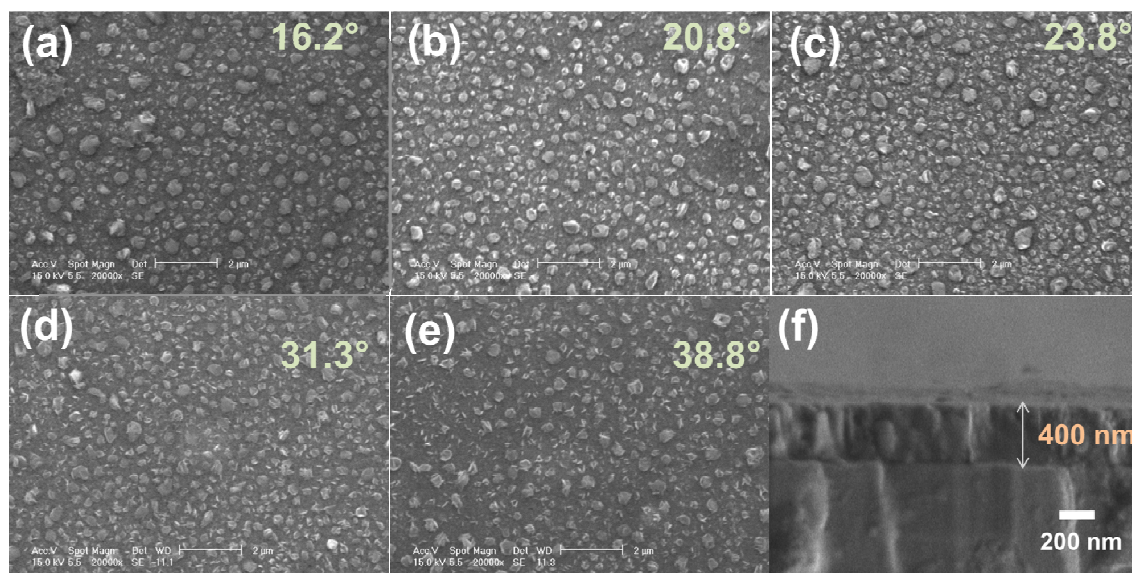


Figure 2. a-d) scanning electron microscopy (SEM) images of the AZO electrodes prepared at target tilt angles from 16.2°-38.8°, respectively, f) cross-sectional image of the AZO electrode of thickness 400 nm confirming the accuracy of the *in-situ* crystal monitoring and that calculated from spectroscopic ellipsometry.

The combined effect of increased carrier concentration and mobility values with smaller target tilt angle resulted in a major improvement in the sheet resistances, which decreased from 544 to $25 \Omega \square^{-1}$. These results are consistent with earlier reports by Treharne et al. [40] where the sheet resistance and Hall-mobility improved with smaller target tilt angles. However, in the work by Treharne et al the electrodes were deposited at 150°C to achieve a low sheet resistance.

From the preceding discussion it can be clearly seen that the target tilt angle is a first order parameter for the preparation of AZO films by sputtering. Improved optoelectronic properties are observed at lower target tilts, e.g., AZO deposited with a tilt angle of 16.2° had a sheet resistance of $25 \Omega \square^{-1}$. However, we found that using such a small target tilt angle gave rise to large variations in the sheet resistances across a film due to film non-uniformity. To this end we found that a target tilt angle of 20.8° gave sufficient uniformity and appropriate sheet resistance and therefore this was chosen as the optimized target tilt angle for the film thickness studies.

3.3 Effect of different film thickness

The sheet resistance, R_{sh} , of a film is inversely proportional to the film thickness (t) and is given by $R_{sh} = \frac{\rho}{t} = \frac{1}{\sigma t}$, [48, 49] where ρ and σ are the resistivity and conductivity of the film, respectively. Therefore, it would be expected that a thicker AZO film would give a lower sheet resistance. On the other hand, a thicker coating also implies less transparency according to the equation, $T = e^{-\alpha t}$, where T is the optical transmission and α is the optical absorption coefficient. The two parameters, T and σ , are dependent on carrier concentration. Decreased T is expected for increased carrier concentration where the main contributors are Al dopants, Al and Zn interstitials [50]. However, for the AZO grown at room temperature the main electron donor contribution comes from oxygen vacancies and therefore importantly the optical absorption is less sensitive to film thickness [34]. In **Table 1**, a 362 nm thick AZO film deposited with target tilt of 20.8° resulted in sheet resistance of $40 \Omega \square^{-1}$. Upon increasing the thickness of AZO film we found it was possible to reduce the sheet resistance to below $10 \Omega \square^{-1}$ (**Table 2**) without significant loss of optical transmission (**Figure 3**).

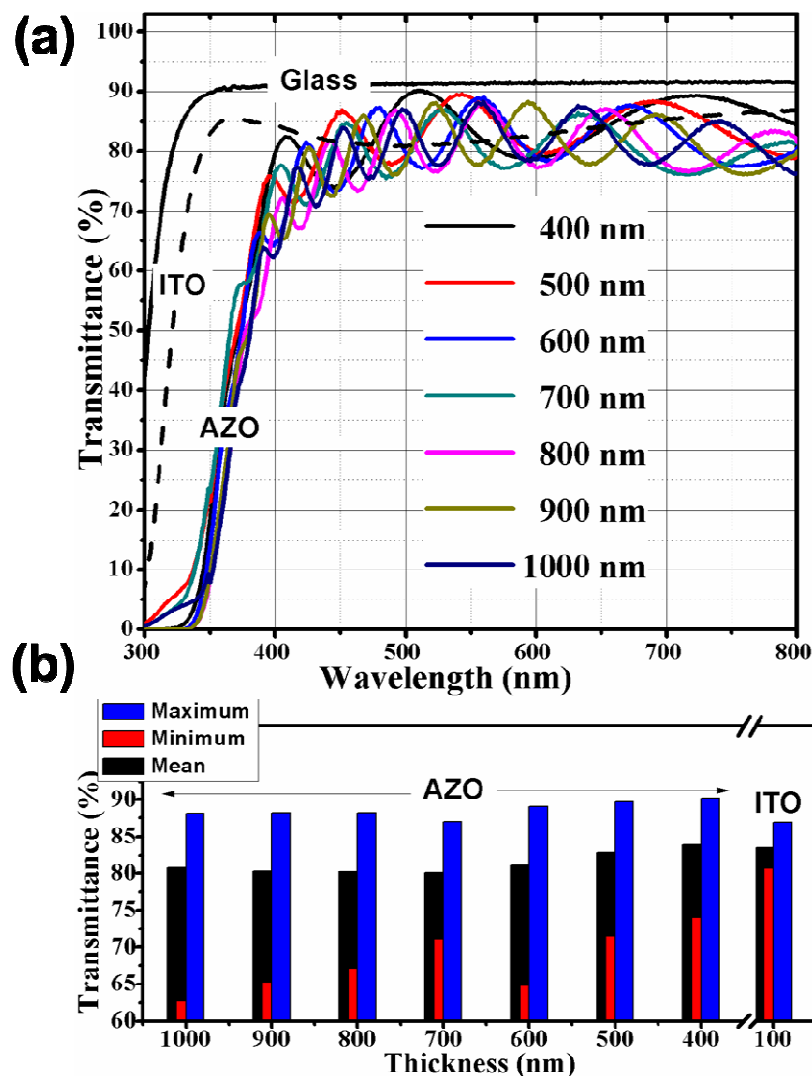


Figure 3. a) Substrate (glass)-corrected optical transmission spectra collected for the AZO films of different thicknesses ranging from 400 nm to 1000 nm, also shown are the substrate (glass) and ITO spectra for comparison. b) Mean, maximum and minimum visible transmittance values calculated in the wavelength range 400 nm to 800 nm of AZO electrodes of different thicknesses and ITO (100 nm thickness).

Variation in the AZO thickness from 400 nm to 1000 nm resulted in a change in the sheet resistance from 30 to $8 \Omega \square^{-1}$ with only a 4% drop in the mean transmission in the visible spectral region (84 to 80%). The electrical parameters from Hall-effect measurements are given in **Table 2** and to our knowledge these are the best optoelectronic parameter combinations yet reported (sheet resistance and optical transmission) for the room-temperature grown AZO electrodes [35-37,51-53].

Table 2. The electrical characteristics of the AZO electrodes in comparison with ITO. Figure of merits calculated using solar-weighted transmission WT (from 350-800 nm) for the AZO electrodes and ITO.

Thickness [nm]	R_{sh} [$\Omega \square^{-1}$]	n [cm⁻³]	μ [cm²V⁻¹ s⁻¹]	ρ [Ω cm]	WT(λ) 350-800	Φ_J
100 (ITO)	18±0.0	1.4×10 ²⁰	37.6	1.8×10 ⁻⁴	83.3	0.30±0.00
1000(AZO)	8.6±0.1	3.6×10 ²⁰	21.0	8.6×10 ⁻⁴	78.8	0.49±0.05
900(AZO)	7.9±0.4	4.1×10 ²⁰	22.6	7.1×10 ⁻⁴	78.7	0.53±0.03
800(AZO)	9.4±0.6	3.7×10 ²⁰	22.9	7.5×10 ⁻⁴	78.3	0.43±0.02
700(AZO)	9.7±0.6	4.0×10 ²⁰	24.6	6.8×10 ⁻⁴	78.8	0.43±0.02
600(AZO)	9.4±0.5	4.5×10 ²⁰	25.1	5.6×10 ⁻⁴	79.6	0.46±0.02
500(AZO)	13±1.0	4.4×10 ²⁰	23.6	6.5×10 ⁻⁴	81.5	0.37±0.02
400(AZO)	31±3.0	2.8×10 ²⁰	16.0	1.2×10 ⁻³	82.0	0.16±0.01

The improved sheet resistance with increased thickness of the electrode as shown in **Table 2** does not have a significant influence on carrier density and mobility once the films are thicker than 500 nm. This arises from the fact that there is insignificant variation in average crystallite size (**Figure S1 and Table S1**, calculated from the XRD study) and also comparable grain size features (see the Atomic Force Microscopy (AFM) images, **Figure 4**) for all AZO films of different thicknesses.

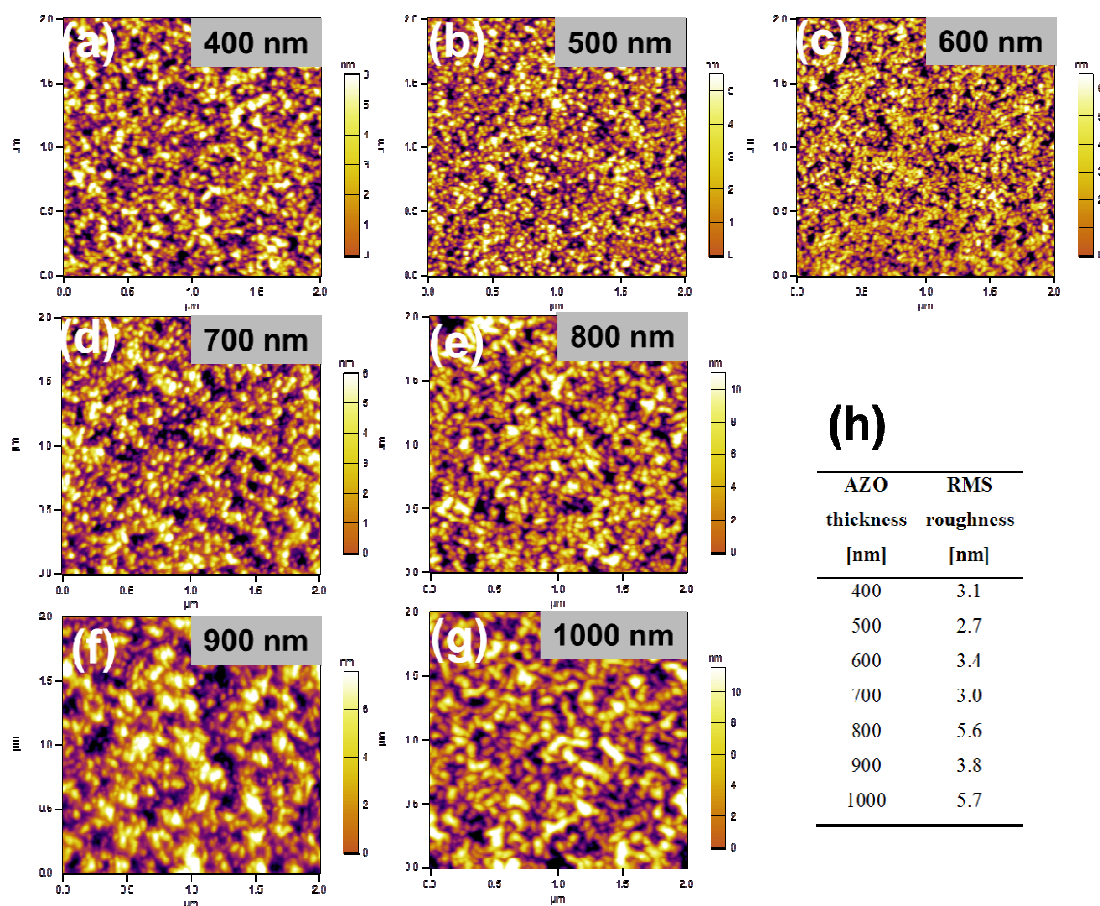


Figure 4. a-g) $2\mu\text{m} \times 2\mu\text{m}$, scale atomic force microscopy (AFM) images of the AZO electrodes with thicknesses ranging from 400-1000 nm, respectively, h) root-mean square (RMS) roughness values of the same.

The carrier densities across all films were essentially the same (of order of 10^{20} cm^{-3}) indicative of similar deposition conditions in all cases. Tanaka et al., [54] observed the same saturation behavior in the electrical properties for thicker AZO films prepared by PLD.

3.4 Electrode quality: Figure of merit calculation

A convenient and accepted tool to compare the optoelectronic properties of transparent conducting electrodes is by using a figure of merit (FOM) [55-57]. FOMs (Φ_f) for AZO electrodes were calculated using the equation defined by Jain et al [49, 58]:

$$\Phi_f = \frac{\sigma}{\alpha} = -[R_s \ln(T + R)]^{-1} \quad (1)$$

where σ is the DC electrical conductivity, α is optical absorption co-efficient, R_s is the sheet resistance, T is the optical transmission and R is the reflection of the TC electrode. R can be neglected as a variable since all oxide transparent electrodes have similar reflection coefficients across the visible region and equation 1 reduces to:

$$\Phi_j = \frac{\sigma}{\alpha} = -[R_s \ln(T)]^{-1} \quad (2)$$

Normally, when calculating an FOM, the optical transmission at a single wavelength is used. For example, in the literature, the transmission at 550 nm (T_{550}) is often taken for this calculation [31], but depending on the application T_{550} is not always a good indicator of the ‘true’ transmission. For example, for OPV devices of interest in this work neither a single wavelength nor a simple average of the transmission spectrum over a given range of wavelengths is suitable. For OPV applications it is best to weight the average of the transmission by the solar photon flux $G(\lambda)$ in order to evaluate the relative quantity of solar photons that will pass through the electrode into the photoactive junction [59]. The solar-weighted transmission ($WT(\lambda)$) is calculated using equation 3, where $G(\lambda)$ is the wavelength-dependent AM 1.5G solar flux, $T(\lambda)$ is the wavelength-dependent electrode transmission, and λ_1 and λ_2 are chosen to correspond to spectral response of the OPV device. The FOMs for AZO electrodes calculated using equation 2 and 3 are given in **Table 2**. λ_1 and λ_2 were chosen as 350 nm and 800 nm, respectively. The FOM of the AZO electrodes were found to be sensitive to the sheet resistance, with the low sheet resistance AZO electrodes having higher FOMs than ITO.

$$WT(\lambda) = \frac{\int_{\lambda_1}^{\lambda_2} G(\lambda)T(\lambda)d\lambda}{\int_{\lambda_1}^{\lambda_2} G(\lambda)d\lambda} \quad (3)$$

3.5. Optical modeling and OPV device performance

Figure 3b shows that the mean transmission in the visible region of AZO electrodes is better for thinner films. However, from **Table 2**, the sheet resistance of the electrodes is superior with thicker AZO films. This trade-off between transmission and sheet resistance is very typical for transparent conducting thin films. To test the optoelectronic properties of this range of AZO electrodes (400 nm – 1000 nm in thickness) OPV devices using a bulk heterojunction blend of poly(3-*n*-hexylthiophene-2,5-diyl) (P3HT) and phenyl-C61-butyric acid methyl ester (PCBM) as the active layer were fabricated. A schematic of device structure is shown in the inset of **Figure 5(a)**.

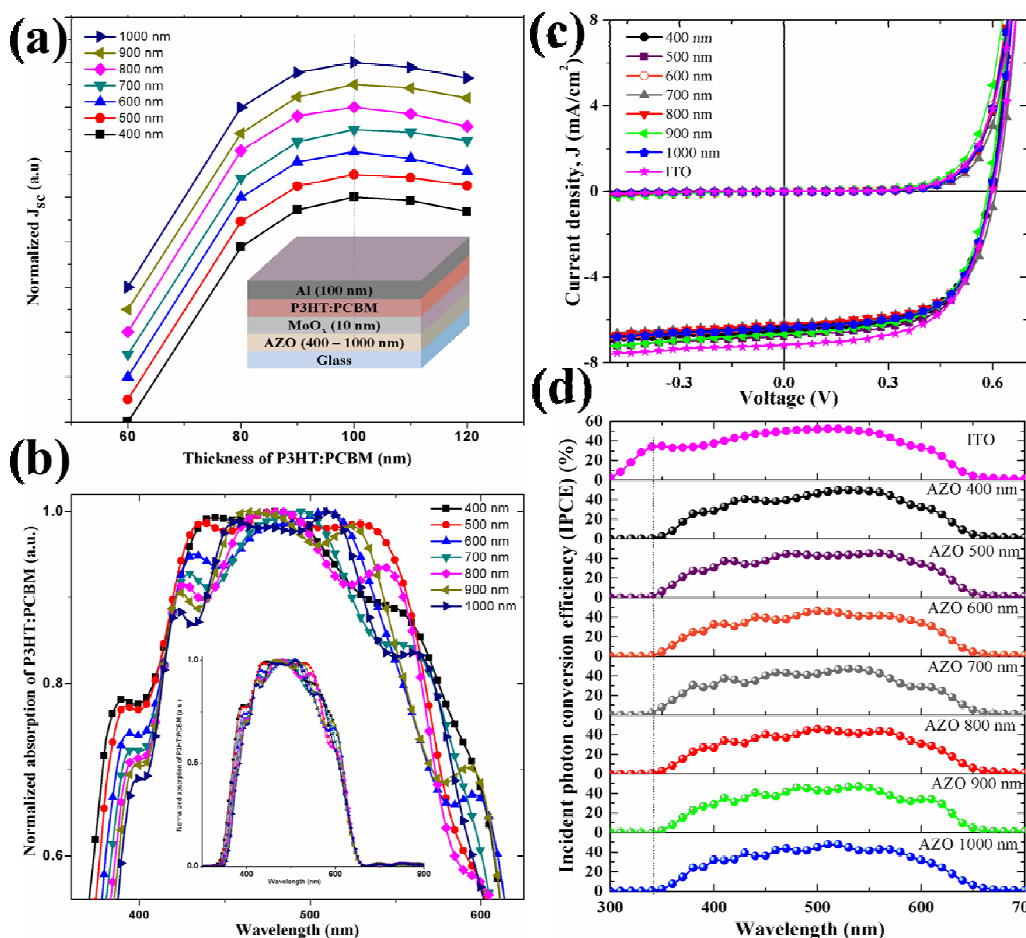


Figure 5. (a) J_{sc} of the OPV devices with various thicknesses of AZO electrodes from optical modelling, and (b) absorption profile of P3HT:PCBM films in devices with different AZO thicknesses at the optimized thickness of the P3HT:PCBM active layer (~100 nm). Inset of (a) shows the OPV device structure and inset of (b) shows the full absorption spectra. (c) Current density versus voltage, and (d) IPCE at different wavelengths of the OPV devices with ITO and different thicknesses of AZO.

To optimize device efficiency, the OPV devices were modelled to achieve maximum short circuit current density (J_{sc}) by varying the thickness of the active layer [60]. An optical-only model was used and the Internal Quantum Efficiency (IQE) was assumed to be 100%. This does not affect the optimization process but over-estimates the current uniformly across the spectral response. **Figure 5a** shows the current density for different thicknesses of P3HT:PCBM and AZO films. It was found that independent of the thickness of the AZO electrodes, the maximum J_{sc} was achieved with a ~100 nm thick P3HT:PCBM active layer. Absorption profiles for devices with a 100 nm thick P3HT:PCBM layer are shown in **Figure 5b**. The number of fringes in the absorption spectra increases with increasing thickness of the AZO layer as the number of optical cavity modes increases for devices with thicker electrodes. The current density–voltage (J - V) characteristics of the best OPV devices with optimized P3HT:PCBM active layer thickness for each AZO thickness are shown in **Figure 5c**. The highest and averages of efficiency, J_{sc} , open circuit voltage (V_{oc}) and fill factor (FF) for each set of devices are given in **Table 3**. For comparison, data on an optimized OPV device on commercial ITO is also included (as are statistics in **Table 3**).

Table 3. The characteristics of OPV devices using AZO electrodes of different thicknesses ranging from 400-1000 nm and the ITO reference device of 100 nm thickness. Values are represented as statistical averages of 5 devices in each category with errors and best value in the parentheses.

Material	J_{sc} (mA/cm ²)	V_{oc} (V)	FF	PCE [%]
AZO(400)	6.2 ± 0.2(6.5)	0.58 ± 0.00(0.58)	0.61 ± 0.01(0.63)	2.2 ± 0.1(2.4)
AZO(500)	6.3 ± 0.3(6.8)	0.58 ± 0.00(0.58)	0.63 ± 0.02(0.64)	2.3 ± 0.1(2.5)
AZO(600)	6.2 ± 0.1(6.4)	0.58 ± 0.00(0.58)	0.63 ± 0.02(0.64)	2.2 ± 0.1(2.4)
AZO(700)	6.0 ± 0.1(6.2)	0.59 ± 0.01(0.60)	0.63 ± 0.01(0.64)	2.2 ± 0.1(2.4)
AZO(800)	6.0 ± 0.1(6.2)	0.58 ± 0.01(0.58)	0.63 ± 0.01(0.64)	2.2 ± 0.1(2.3)
AZO(900)	6.3 ± 0.2(6.7)	0.57 ± 0.01(0.58)	0.62 ± 0.01(0.63)	2.2 ± 0.1(2.3)
AZO(1000)	6.3 ± 0.2(6.4)	0.57 ± 0.01(0.58)	0.63 ± 0.01(0.64)	2.3 ± 0.1(2.4)
ITO(100)	6.9 ± 0.2(7.2)	0.58 ± 0.01(0.58)	0.61 ± 0.01(0.61)	2.4 ± 0.1(2.6)

From **Figure 5c**, it is seen that the J-V curves of devices for all AZO thicknesses are similar. This is also seen in the averages of the performance parameters given in **Table 3**. Efficiency, J_{sc} , V_{oc} and FF remain the same within error (standard deviations) across all thicknesses of the AZO electrodes. The reduction in average optical transmittance, (**Figure 3b**) with higher AZO electrode thickness is compensated by improved electrical properties (**Table 2**), and therefore, the efficiency remains essentially the same up to an AZO thickness of 1000 nm. The efficiency of the best OPV devices with an AZO electrode reached ~98% of the best efficiency of the reference ITO device and ~94% on average. The slightly better efficiency of the ITO device mainly arises from a higher J_{sc} . The other critical parameters (V_{oc} , FF) are very similar between the AZO and ITO based devices (**Table 3**). The higher J_{sc} of the ITO device is easily explained by the broader and slightly higher incident photon quantum yield (IPCE – or External Quantum Efficiency) profile of ITO devices as shown in **Figure 5d**. The IPCE spectrum for ITO rises at lower wavelengths relative to the AZO electrodes, as expected, because the band gap of ITO is ~3.5 eV (350 nm) whereas AZO has a band gap of ~3.1 eV (400 nm) as shown in (**Figure 3a**). The J_{sc} calculated by integrating the convolution of the IPCE and AM 1.5 solar spectrum showed ~ 10% higher J_{sc} for ITO devices compared to AZO devices, which agrees closely with the difference in J_{sc} measured under white light (**Table 3**, ~ 9% difference in J_{sc} of OPV on ITO and AZO 500 nm). This observation validates our solar cell measurements.

4. Conclusions

The target tilt angle has been identified as an important parameter to achieve state-of-the-art optoelectronic properties of AZO TCO electrodes deposited by the industrially viable magnetron sputtering technique. By varying the target tilt angle the best yet reported optical-electrical combination properties for AZO electrodes were achieved. The room temperature deposited AZO electrodes had R_{sh} reduced from 30 to $8 \Omega \square^{-1}$ as the thickness was increased from 400 nm to 1000 nm, with only a 4% drop in the transmission (84 to 80%) in visible region. Furthermore, application of the AZO electrodes in OPV devices successfully demonstrated that their performance is comparable to devices that use commercial ITO. These results demonstrate the applicability of room temperature grown AZO electrodes as an alternative to ITO in organic optoelectronics device applications.

Acknowledgements

This work was supported by the CSIRO Future Manufacturing Flagship: Flexible Transparent Electrodes for Plastic Electronics Cluster which includes The University of Queensland, University of Technology, Sydney and Flinders University. Fabrication and testing were done in part at the Queensland node of the Australian National Fabrication Facility (ANFF-Q). PLB and PM are University of Queensland Senior Research Fellows and PM is also an ARC Discovery Outstanding Researcher Awardee.

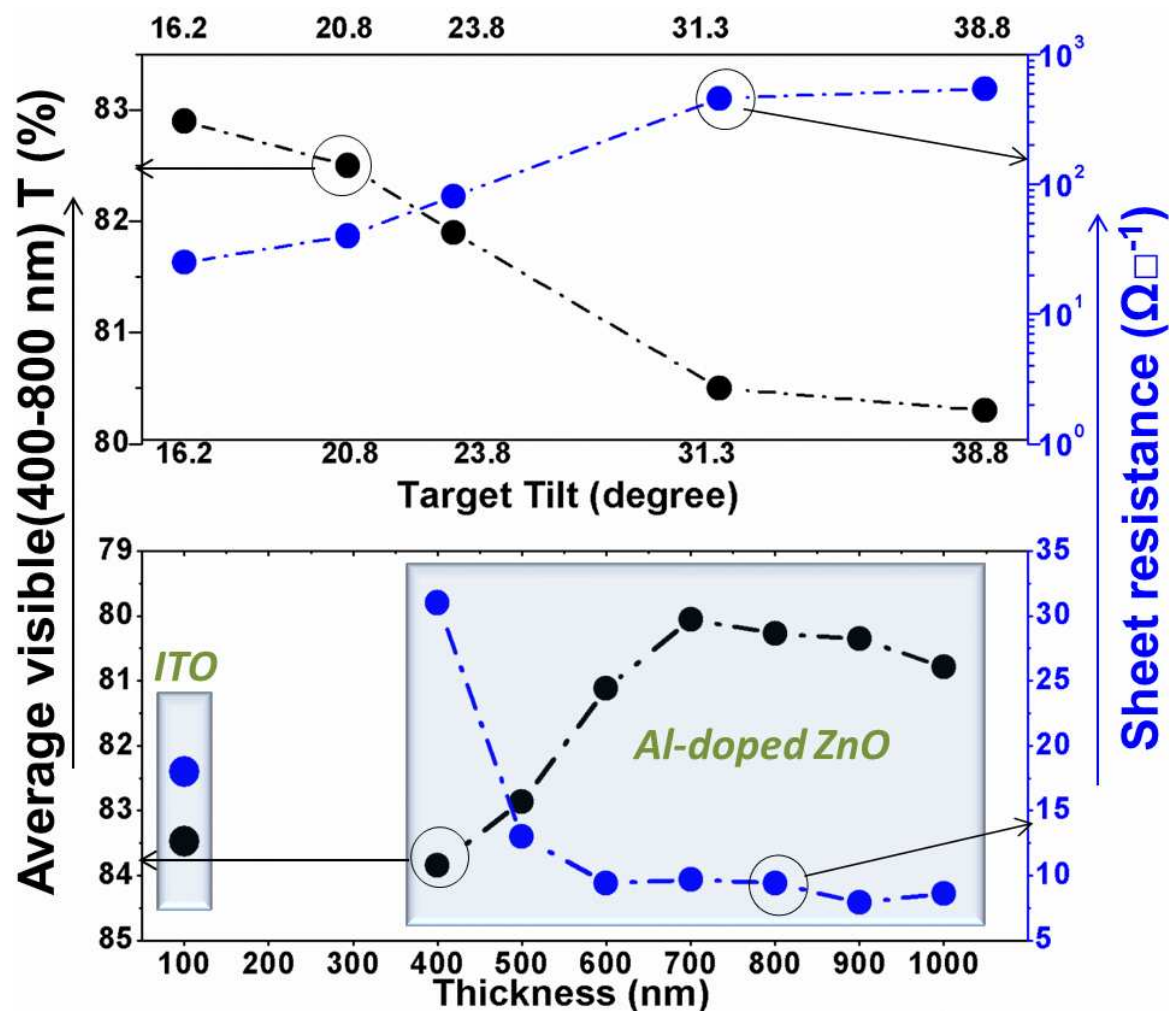
References

- 1 F. Zhang, X. Xu, W. Tang, J. Zhang, Z. Zhuo, J. Wang, J. Wang, Z. Xu and Y. Wang, *Solar Energy Materials and Solar Cells*, 2011, **95**, 1785-1799.
- 2 I. Etxebarria, J. Ajuria and R. Pacios, *Organic Electronics*, 2015, **19**, 34-60.
- 3 K.A. Mazzi and C.K. Luscombe, *Chemical Society Reviews*, 2015, **44**, 78-90.
- 4 G.L. Ingram and Z.-H. Lu, *Journal of Photonics for Energy*, 2014, **4**, 040993-040993.
- 5 M.C. Gather, A. Köhnen and K. Meerholz, *Advanced Materials*, 2011, **23**, 233-248.
- 6 K. Ellmer, *Nature Photonics*, 2012, **6**, 809-817.
- 7 M.W. Rowell and M.D. McGehee, *Energy & Environmental Science*, 2011, **4**, 131-134.
- 8 A. Singh, R. Mehra, N. Buthrath, A. Wakahara and A. Yoshida, *Journal of Applied Physics*, 2001, **90**, 5661-5665.
- 9 K. Mahmood and S. B. Park, *Electronic Materials Letters*, 2013, **9**, 161-170.
- 10 W.-J. Jeong and G.-C. Park, *Solar energy materials and solar cells*, 2001, **65**, 37-45.
- 11 M. Hamsch, H. Jin, A. J. Clulow, A. Nelson, N. L. Yamada, M. Velusamy, Q. Yang, F. Zhu, P. L. Burn and I. R. Gentle, *Solar Energy Materials and Solar Cells*, 2014, **130**, 182-190.
- 12 S. D. Yambem, M. Ullah, K. Tandy, P. L. Burn and E. B. Namdas, *Laser & Photonics Reviews*, 2014, **8**, 165-171.
- 13 C.-H. Lee, R. Pandey, B.-Y. Wang, W.-K. Choi, D.-K. Choi and Y.-J. Oh, *Solar Energy Materials and Solar Cells*, 2015, **132**, 80-85.
- 14 J. Zou, C. Z. Li, C. Y. Chang, H. L. Yip and A. K. Y. Jen, *Advanced Materials*, 2014, **26**, 3618-3623.
- 15 R. Pandey, B. Angadi, S. K. Kim, J. W. Choi, D. K. Hwang and W. K. Choi, *Optical Materials Express*, 2014, **4**, 2078-2089.
- 16 A. J. Stapleton, R. A. Afre, A. V. Ellis, J. G. Shapter, G. G. Andersson, J. S. Quinton and D. A. Lewis, *Science and Technology of Advanced Materials*, 2013, **14**, 035004.
- 17 B. Han, K. Pei, Y. Huang, X. Zhang, Q. Rong, Q. Lin, Y. Guo, T. Sun, C. Guo and D. Camahan, *Advanced Materials*, 2014, **26**, 980-980.
- 18 K. Zilberberg, F. Gasse, R. Pagui, A. Polywka, A. Behrendt, S. Trost, R. Heiderhoff, P. Görrn and T. Riedl, *Advanced Functional*

- Materials*, 2014, **24**, 1650-1650.
- 19 K. Zilberberg, F. Gasse, R. Pagui, A. Polywka, A. Behrendt, S. Trost, R. Heiderhoff, P. Görrn and T. Riedl, *Advanced Functional Materials*, 2014, **24**, 1671-1678.
- 20 P.-C. Hsu, S. Wang, H. Wu, V. K. Narasimhan, D. Kong, H. R. Lee and Y. Cui, *Nature communications*, 2013, **4**.
- 21 H. Wu, D. Kong, Z. Ruan, P.-C. Hsu, S. Wang, Z. Yu, T. J. Carney, L. Hu, S. Fan and Y. Cui, *Nature nanotechnology*, 2013, **8**, 421-425.
- 22 H. Hosono, *Nature chemistry*, 2012, **4**, 252-253.
- 23 H. Mizoguchi, T. Kamiya, S. Matsuishi and H. Hosono, *Nature communications*, 2011, **2**, 470.
- 24 M. Neubert, S. Cornelius, J. Fiedler, T. Gebel, H. Liepack, A. Kolitsch and M. Vinnichenko, *Journal of Applied Physics*, 2013, **114**, 083707.
- 25 A. Walsh, A. B. Kehoe, D. J. Temple, G. W. Watson and D. O. Scanlon, *Chemical Communications*, 2013, **49**, 448-450.
- 26 H. Hosono, M. Yasukawa and H. Kawazoe, *Journal of non-crystalline solids*, 1996, **203**, 334-344.
- 27 Z. Yan, H. Takei and H. Kawazoe, *Journal of the American Ceramic Society*, 1998, **81**, 180-186.
- 28 T. Minami, *Thin Solid Films*, 2008, **516**, 1314-1321.
- 29 A. Kasry, M. A. Kuroda, G. J. Martyna, G. S. Tulevski and A. A. Bol, *ACS nano*, 2010, **4**, 3839-3844.
- 30 X. Wang, L. Zhi and K. Müllen, *Nano letters*, 2008, **8**, 323-327.
- 31 Y. H. Kim, J. S. Kim, W. M. Kim, T. Y. Seong, J. Lee, L. Müller-Meskamp and K. Leo, *Advanced Functional Materials*, 2013, **23**, 3645-3652.
- 32 J. E. Medvedeva, *Applied Physics A*, 2007, **89**, 43-47.
- 33 B. Liu, M. Gu, X. Liu, S. Huang and C. Ni, *Applied Physics Letters*, 2010, **97**, 122101-122103.
- 34 J. E. Medvedeva and C. L. Hettiarachchi, *Physical Review B*, 2010, **81**, 125116.
- 35 H. Hagendorfer, K. Lienau, S. Nishiwaki, C. M. Fella, L. Kranz, A. R. Uhl, D. Jaeger, L. Luo, C. Gretener and S. Buecheler, *Advanced Materials*, 2014, **26**, 632-636.
- 36 J. B. Franklin, J. B. Gilchrist, J. M. Downing, K. A. Roy and M. A. McLachlan, *Journal of Materials Chemistry C*, 2014, **2**, 84-89.
- 37 J.-A. Jeong, H.-S. Shin, K.-H. Choi and H.-K. Kim, *Journal of Physics D: Applied Physics*, 2010, **43**, 465403.
- 38 Y. S. Jung, H. W. Choi, K. H. Kim, S. J. Park and H. H. Yoon, *Journal of the Korean Physical Society*, 2009, **55**, 1945-1949.
- 39 R. E. Trehame, K. Hutchings, D. A. Lamb, S. J. C. Irvine, D. Lane and K. Durose, *Journal of Physics D: Applied Physics*, 2012, **45**, 335102.
- 40 G. F. Burkhard, E. T. Hoke and M. D. McGehee, *Advanced Materials*, 2010, **22**, 3293-3297.
- 41 L. A. Pettersson, L. S. Roman and O. Inganäs, *Journal of Applied Physics*, 1999, **86**, 487-496.
- 42 A. A. Mosquera, D. Horwat, A. Rashkovskiy, A. Kovalev, P. Miska, D. Wainstein, J. M. Albella and J. L. Endrino, *Scientific reports*, 2013, **3**.
- 43 R. P. Vinci and J. J. Vlassak, *Annual Review of Materials Science*, 1996, **26**, 431-462.
- 44 B. D. Cullity and S. R. Stock, *Elements of X-ray Diffraction*, Pearson, 2001.
- 45 R. Cebulla, R. Wendt and K. Ellmer, *Journal of applied physics*, 1998, **83**, 1087-1095.
- 46 J. Lu, S. Fujita, T. Kawaharamura, H. Nishinaka, Y. Kamada, T. Ohshima, Z. Ye, Y. Zeng, Y. Zhang and L. Zhu, *Journal of Applied Physics*, 2007, **101**, 083705.
- 47 M. Chen, Z. Pei, X. Wang, C. Sun and L. Wen, *Journal of Vacuum Science & Technology A*, 2001, **19**, 963-970.
- 48 D. K. Schroder, *Semiconductor material and device characterization*, John Wiley & Sons, 2006.
- 49 V. K. Jain and A. P. Kulshreshtha, *Solar Energy Materials*, 1981, **4**, 151-158.
- 50 Y.-S. Kim and C. Park, *Physical review letters*, 2009, **102**, 086403.
- 51 M. Agarwal, P. Modi and R. Dusane, *J. Nano-Electron Phys.*, 2013, **5**, 02027
- 52 Y. Wang, J. Lu, X. Bie, L. Gong, X. Li, D. Song, X. Zhao, W. Ye and Z. Ye, *Journal of Vacuum Science & Technology A*, 2011, **29**, 031505.
- 53 V. Sittinger, F. Ruske, W. Werner, C. Jacobs, B. Szyszka and D. Christie, *Thin Solid Films*, 2008, **516**, 5847-5859.
- 54 H. Tanaka, K. Ihara, T. Miyata, H. Sato and T. Minami, *Journal of Vacuum Science & Technology A*, 2004, **22**, 1757-1762.
- 55 G. Haacke, *Journal of Applied Physics*, 1976, **47**, 4086-4089.
- 56 S. De, T. M. Higgins, P. E. Lyons, E. M. Doherty, P. N. Nirmalraj, W. J. Blau, J. J. Boland and J. N. Coleman, *ACS nano*, 2009, **3**, 1767-1774.

- 57 Á. Pekker and K. Kamaras, *Journal of Applied Physics*, 2010, **108**, 054318.
- 58 R. G. Gordon, *MRS bulletin*, 2000, **25**, 52-57.
- 59 T. M. Barnes, M. O. Reese, J. D. Bergeson, B. A. Larsen, J. L. Blackburn, M. C. Beard, J. Bult and J. van de Lagemaat, *Advanced Energy Materials*, 2012, **2**, 353-360.
- 60 A. Armin, M. Velusamy, P. Wolfer, Y. Zhang, P. L. Burn, P. Meredith and A. Pivrikas, *ACS Photonics*, 2014, **1**, 173-181.

Table of Contents Graph & Text:



Target tilted room temperature sputtering of aluminum doped zinc oxide (AZO) provides transparent conducting electrodes with sheet resistances of $<10 \Omega \square^{-1}$ and average transmittance in the visible of 80-84%. The properties of the AZO electrode are found to be strongly dependent on the target-tilting angle and film thickness. The AZO electrodes showed comparable performance to commercial indium tin oxide (ITO) electrodes in organic photovoltaic (OPV) devices. These results demonstrate that AZO films are a good alternative to ITO for transparent conducting electrodes for organic optoelectronic applications.